Nanoscale

PAPER

View Article Online
View Journal | View Issue

Cite this: *Nanoscale*, 2024, **16**, 11274

Carriers for hydrophobic drug molecules: lipid-coated hollow mesoporous silica particles, and the influence of shape and size on encapsulation efficiency†

Sumiya Iqbal, [a] Tom-Jonas Klaus Schneider, [a] Thanh Tung Truong,[d] Roman Ulrich-Müller,[b,c] Phuong-Hien Nguyen,[d] Shaista Ilyas *[a] and Sanjay Mathur *[a]

Hydrophobic drugs, while designed to interact with specific receptors or enzymes located in lipid-rich cell membranes, often face challenges of limited bioavailability and insufficient circulation time due to their insolubility in aqueous environments. One plausible pathway to increase their blood circulation time is to load these drugs into biocompatible and hydrophilic carriers to enhance their uptake. In this study, mesoporous silica ($mSiO_2$) nanocarriers of various morphologies (including cubes, capsules, and spheres) were synthesized. These nanocarriers were then surface-functionalized with alkyl chain hydrocarbons, specifically octadecyl-trimethoxysilane, $(OCH_3)_3Si(CH_2)_{17}CH_3$, to render them hydrophobic. The resulting nanocarriers ($((OCH_3)_3Si(CH_2)_{17}CH_3)@mSiO_2$) showed up to 80% uptake for hydrophobic drugs. However, a significant drawback was observed as most of the drugs were prone to uncontrollable release within 6 h. This challenge of premature drug release was successfully mitigated by effectively sealing the drug-loaded nanocarriers with a pH-sensitive lipid overlayer. The lipid-coated nanocarriers prolonged drug containment and sustained release up to 72 h, compared to 6 h for uncoated nanocarriers, thereby facilitating longer blood circulation times. Moreover, the shape and size of nanocarriers were found to influence both drug entrapment capacity and release behavior with cubic forms exhibiting superior loading capacity due to higher surface area and porosity. Additionally, it was observed that the molecular weight and chemical structure of the drug molecules played a crucial role in determining their uptake and release profiles. Furthermore, the influence of different morphologies of nanocarriers on cell uptake and cytotoxicity in immune cells was elucidated. These findings underscore the importance of nanocarrier morphology and drug properties to enhance loading capacities and controlled release profiles, for designing drug delivery systems tailored for hydrophobic drugs.

Received 31st March 2024,
Accepted 13th May 2024

DOI: 10.1039/d4nr01420k

rsc.li/nanoscale

Introduction

Many anticancer drugs including bosutinib, dasatinib, tamoxifen, and curcumin are hydrophobic, leading to poor retention times within the human body.[1–5] Given their chemical design to favorably interact with specific receptors located in the lipid-rich cell membrane or intracellular compartments of cells, it is imperative to discover new carrier systems enabling their optimum encapsulation and transport.[6–10] Ultrafine carriers capable of containing hydrophobic molecules are ideally suited to enhance blood circulation and drug uptake. Several nanocarriers have been extensively studied for their efficiency in drug delivery, particularly in enhancing therapeutic bioavailability and targeting precision such as liposomes, which are notable for their ability to encapsulate both hydrophilic and hydrophobic drug molecules, offering versatile delivery mechanisms.[11] Similarly, polymeric/lipid nanoparticles, particularly those made from biodegradable materials like polylactic-*co*-glycolic acid or tricaprylate, provide controlled release properties.[12,13] Additionally dendrimers, with their unique, highly branched structures and metallic nanoparticles such as gold and silver allow for precise

[a]*Institute of Inorganic and Materials Chemistry, University of Cologne, Greinstr. 6, 50939 Cologne, Germany. E-mail: sanjay.mathur@uni-koeln.de*
[b]*Department II of Internal Medicine and Center for Molecular Medicine Cologne, University of Cologne, Faculty of Medicine and University Hospital Cologne, Cologne, Germany*
[c]*University of Cologne, Faculty of Medicine and University Hospital Cologne, Cluster of Excellence Cellular Stress Responses in Aging-associated Diseases (CECAD), Joseph-Stelzmann-Straße 26, 50931, Cologne Germany*
[d]*University of Cologne, Faculty of Medicine and University Hospital Cologne, Department I of Internal Medicine; Center for Molecular Medicine Cologne, Kerpener Str. 62, 50937 Cologne, Germany*

†Electronic supplementary information (ESI) available: Fig. S1–S6. See DOI: https://doi.org/10.1039/d4nr01420k

functionalization and drug encapsulation.[14,15] In the realm of these nanocarriers, mesoporous silica ($mSiO_2$) has emerged as a promising candidate for *in vivo* drug transport due to its stability, porous surface, high surface area, biocompatibility, degradability and sustained retention time in the body.[16–18] Despite being hydrophilic because of surface hydroxyl groups, entrapment of hydrophobic drugs in silica nanocarriers can be achieved by adjusting their physiochemical nature and pore size, which allows a controlled and sustained drug release.[19–21] Surface functionalization with small molecules, such as estrogen molecules has been shown to enhance drug entrapment in nanocarriers.[22] However, a challenge of mesoporous silica nanocarriers is their leaky nature, resulting in premature drug release in the medium.[23] In such cases, an additional stimuli-responsive overlayer, such as lipid or polymer, can offer better control over the sustained release of drugs from nanocarriers (Fig. 1).[24–27]

This study evaluated the effect of lipid coating as a (surface) sealing mechanism on hydrophobic silica nanocarriers, followed by an examination of hydrophobic drug encapsulation and their release studies. In this study, Tamoxifen was selected as the model drug for encapsulation within our synthesized nanocarriers due to its small structure and its clinical relevance in the treatment of hormone receptor-positive breast cancer.[28] Additionally, the variation in drug entrapment efficiencies was investigated to study the effect of the shapes of silica carriers (spheres, capsules, cubes) and the molecular weight (low *vs.* high) of the drugs. Furthermore, the study elucidated how morphological alterations of nanocarriers impact their interactions with immune cells derived from three healthy donors.

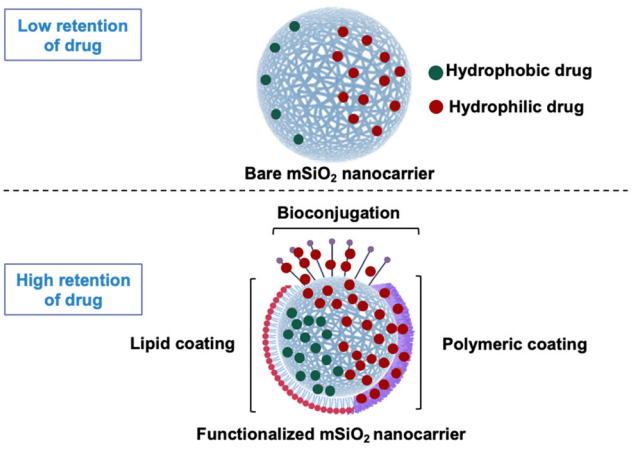

Fig. 1 Enhanced drug entrapment and controlled release can be achieved through bioconjugation on $mSiO_2$. $mSiO_2$ exhibits a strong affinity for hydrophilic drugs, however, it suffers from low retention time, whereas hydrophobic drugs tend to adsorb on the surface, resulting in its limited drug entrapment. The implementation of bioconjugation and polymeric, or lipid coating, offers a promising approach for achieving high retention followed by a controlled and sustained drug release.

Results and discussion

Design and synthesis of nanocarriers

In a typical synthesis, a solid nanoparticle (*e.g.*, Fe_2O_3) is used as a sacrificial template, which is overlayered with silica using sol–gel synthesis.[29–31] Consequently, the solid template is removed by aqueous chemical etching (*i.e.*, HCl) to obtain mesoporous nanocarriers as outlined in Fig. S1.† $mSiO_2$ with a narrow particle size distribution (60 nm (nanospheres and nanocubes), and 400 nm (nanocapsules)) were synthesized with a silica shell thickness of 15 nm and 25 nm for nanocubes and nanocapsules, respectively. Silica carriers adapted the shape of their core material (cube and capsules) as confirmed by scanning electron microscopy (Fig. 2 and S2†). The etching process offered purified amorphous mesoporous nanocarriers (nanocubes and nanocapsules), demonstrating the complete removal of crystalline Fe_2O_3 nanoparticles (Fig. 3).[32] The FTIR analysis showed absorption bands at 1073 cm^{-1}, 960 cm^{-1}, and 800 cm^{-1} corresponding to Si–O–Si stretches (Fig. 4).[33,34]

The adsorption–desorption isotherms for the nanocarriers are shown in Fig. 5. The proximity of the adsorption (black squares) and desorption (red circles) curves indicate a type IV isotherm with hysteresis, characteristic of mesoporous materials as per the IUPAC classification. The isotherm demonstrates monolayer-multilayer adsorption followed by capillary condensation, with a gradual increase in the quantity of nitrogen adsorbed as the relative pressure (P/P_0) rises. The presence of hysteresis suggests capillary condensation within the pores, indicating their uniform size. NLDFT calculations were conducted to ascertain the pore size distribution and total pore volume for all nanocarriers.

For spherical nanocarriers, a pore size of approximately 40 Å (4 nm) and a total pore volume of 0.08 $cm^3\ g^{-1}$ were calculated. In the case of cubes, the pore size was determined to be around 36 Å (3.6 nm) with a total pore volume of 0.25 $cm^3\ g^{-1}$. For the ellipsoid, the pore size was estimated to be around 40 Å with a total pore volume of 0.05 $cm^3\ g^{-1}$. These results demonstrate the porous nature and high surface area of the as-prepared nanocarriers, which aligns well with TEM images demonstrating their porous structures. The surface area, as determined by BET measurements, revealed a high specific surface area of 323.8 $m^2\ g^{-1}$ for ellipsoidal shapes, 88 $m^2\ g^{-1}$ for spherical shapes, and 581.477 $m^2\ g^{-1}$ for cubes (Fig. 6).[35–37]

Surface functionalization of $mSiO_2$

To obtain a hydrophobic surface, octadecyltrimethoxysilane (OTMS) was covalently attached to the surface of mesoporous silica particles based on a condensation reaction, Scheme 1. The FITR data showed the absence of the Si–OH band after their functionalization with silane (Fig. 4). The hydrophobicity of nanocarriers was evaluated by dispersing them in water, where a distinct phase separation was observed as compared to unfunctionalized (well-dispersed) nanocarriers, indicating

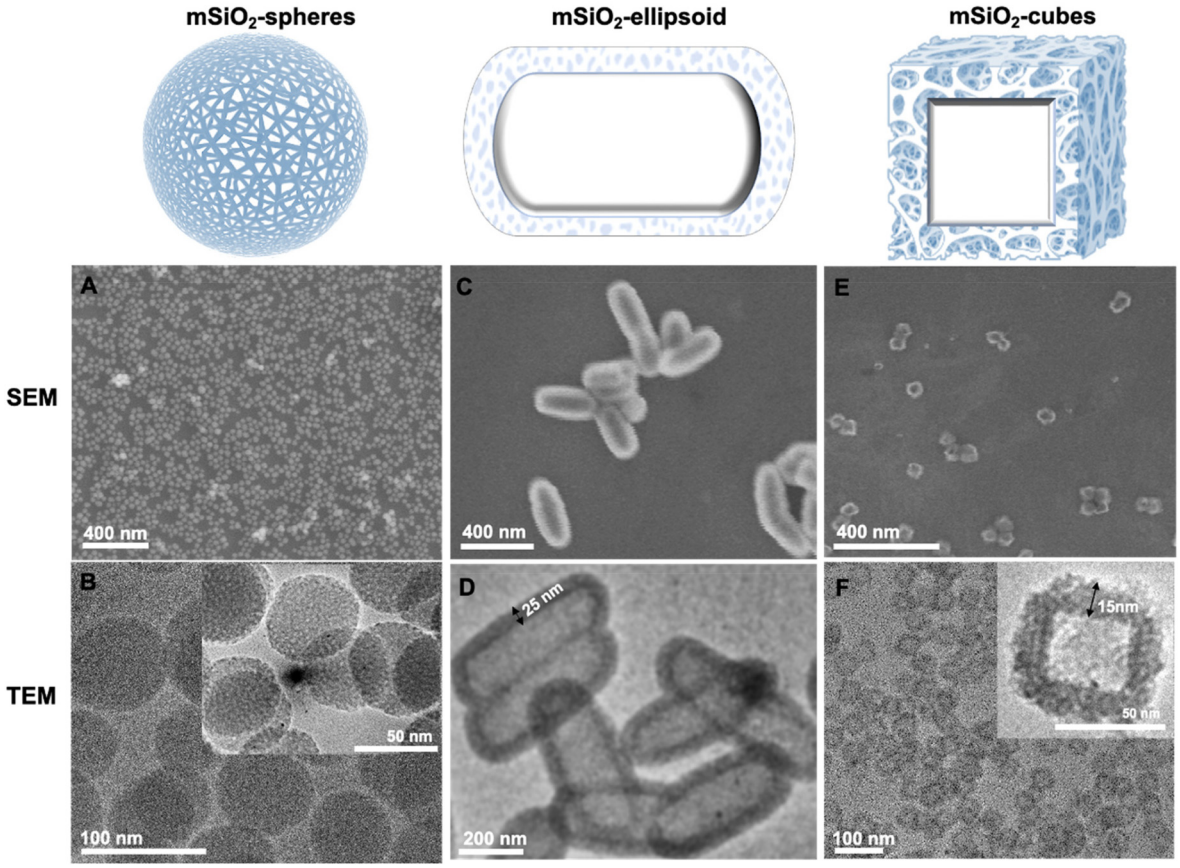

Fig. 2 Morphological evaluation of mesoporous silica nanocarriers by SEM and TEM. (A) Overview SEM image shows monodispersed 60 nm spherical $mSiO_2$. (B) Detailed TEM image clearly shows the porous structure of these spherical $mSiO_2$ (C and D) hollow silica ellipsoid (300 nm) with 25 nm shell and 117 nm hollow cavity. (E and F) Mesoporous nanocubes (60 nm) with a 40 nm hollow cavity and 15 nm porous silica shell.

the hydrophobic nature after the conjugation of silane molecules (Fig. 7).

Drug loading and release study

Synthesized $mSiO_2$ nanocarriers were functionalized with a silane linker to facilitate the encapsulation of hydrophobic drugs. This functionalization was achieved through the conjugation of the $mSiO_2$ surface with the long alkyl hydrocarbon chain *via* a covalent bond, tailored to interact specifically with the hydrophobic regions of the drug molecules. Following the conjugation of the silane linker, the drug was loaded into the mesopores of the $mSiO_2$ driven by hydrophobic interactions between the drug molecules and the modified surfaces of the pores, facilitating efficient encapsulation within the porous structure. This encapsulation process was optimized by adjusting parameters such as the drug-to-linker ratio to maximize loading capacity. After the drug was successfully loaded into the pores, the nanocarriers were coated with a lipid layer. This lipid coating was applied to stabilize the nanocarriers by providing a hydrophilic barrier, which prevents aggregation and acts as a gate keeper for the encapsulated drug.

Influence of surface ligands. To demonstrate the effect of surface-attached hydrophobic linkers, a fixed quantity of described nanocarriers were functionalized with different amounts of OTMS linkers. Following this step, nanocarriers with different densities of surface ligands were exposed to a 0.15 mmol solution of tamoxifen for uptake studies. The interrelation of linker chemistry and drug uptake in the $mSiO_2$ nanocarriers showed a nonlinear behavior with a threshold observed at 12 mmol (50 μl), 47 mmol (200 μl), and 6 mmol (25 μl) for nanospheres, nanocubes, and nanoellipsoids respectively of OTMS concentration with maximum tamoxifen uptake. Upon increasing the OTMS concentration (up to 118 mmol (500 μl)) the drug uptake capacity was gradually decreased to become a minimum at 118 mmolar (500 μl) (Fig. 8 and Fig. S3, S4†). This observation can be explained by the steric congestion caused by the higher density of the surface-rooted OTMS ligands that are inhibitive for the penetration of tamoxifen molecules in the pores of $mSiO_2$ carriers.

Influence of nanocarrier morphology. To investigate the influence of the morphology of nanocarriers, three different shapes were comparatively analyzed in terms of their drug uptake capacity. For this purpose, spherical, ellipsoidal, and cube-shaped $mSiO_2$ nanocarriers were functionalized with the optimized amount of OTMS linker, and drug uptake was conducted with a constant quantity (0.15 mmolar) of tamoxifen in

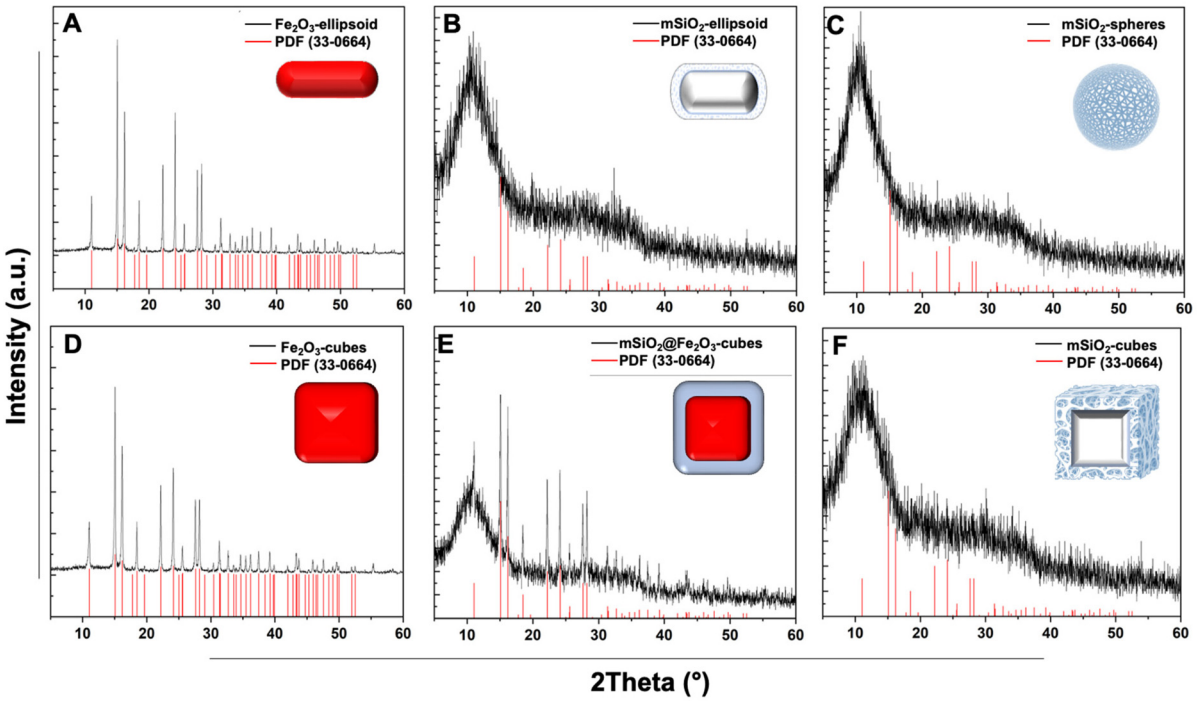

Fig. 3 X-ray diffraction pattern of nanocarriers with the reference of JCPDS pdf no. 33–0064 (red line). (A) α-Fe_2O_3 capsules (black) confirming the formation of hematite nanoparticles. (B) Shows the diffraction pattern mesoporous silica ellipsoid (black) confirming the successful removal of the iron oxide core. (C) Spherical mesoporous silica nanoparticles, indicating the presence of amorphous silica. (D) Presents the pattern for α-Fe_2O_3 nanocubes (black) indicating the formation of hematite nanocubes. (E) Core–shell SiO_2@Fe_2O_3 with the addition of a broad peak, representing the incorporation of amorphous material. (F) Mesoporous silica cubes confirming the removal of the iron oxide core.

all three cases. Tamoxifen loading studies revealed that nanocubes showed the highest drug entrapment efficiency of 84%, nanospheres showed 56% entrapment efficiency, whereas nanoellipsoids showed the lowest entrapment efficiency of 23% (Fig. 9). Since the size of nanoellipsoids is larger than nanocubes, the difference in loading capacity can also be due to the difference in surface area.[38,39] Our results demonstrate that nanocubes are superior drug-loaded carriers as compared to other carriers due to their large surface and pore volume as calculated by BET analysis (Fig. 6). In the case of spheres, it was observed that spherical $mSiO_2$ exhibited higher drug encapsulation efficacy compared to ellipsoid which signifies the role of morphology in encapsulation. This difference can be explained by the higher pore volume of spheres (0.08 $cm^3\ g^{-1}$) as compared to ellipsoids (0.05 $cm^3\ g^{-1}$). Moreover, the small size of spheres (60 nm) compared to ellipsoids (200 × 100 nm) leads to a higher surface-to-volume ratio which would provide a larger surface area for the drug molecules to adhere.

The drug release profile of these nanocarriers showed that within 6 h, the majority of the drug was completely released from all nanocarriers (Fig. 9B). This necessitates a sealant layer that can prolong the drug release time and avoid uncontrolled drug release since a sustained release is ideal for achieving optimal distribution of the drug in the bloodstream.

To withhold the drug in $mSiO_2$ carriers, a lipid coating was applied, and drug release efficiency was studied under the influence of pH stimuli by varying the pH (7.4 and 5.4) at 37 °C (Fig. 10). A pH-dependent release behavior was evident in all cases with lipid-coated $mSiO_2$ carriers. Upon monitoring drug release profiles for 72 h, it was observed that at pH 5.4 (acidic), 75% of drug release occurred. In the case of basic media (pH 7.4), up to 30% release was observed. This selective release at pH 5.4 is attributed to the protonation of the lipid coating at acidic pH, which disrupts the lipid matrix, increasing its permeability. Consequently, the loosened structure facilitates the diffusion of the encapsulated drug out of the nanocarriers. Such pH sensitivity allows the nanocarriers to release their drug payload specifically in the acidic tumor microenvironment to possibly achieve higher drug concentrations in the tumor tissues while minimizing exposure to healthy tissues.[40–42]

Influence of molecular weight and hydrophobicity of drugs. To optimize the drug release profile of hydrophobic drugs, the influence of molecular weight (MW) and hydrophobicity of drugs are important considerations. Therefore, drug entrapment on $mSiO_2$ nanospheres using a series of hydrophobic drugs with different molecular weight and hydrophobicity was conducted using **tamoxifen** (MW: 371 Da), **dasatinib** (MW: 488 Da), **bosutinib** (MW: 530 Da) and **everolimus** (MW: 958 Da). The above-selected compounds represent clinically approved

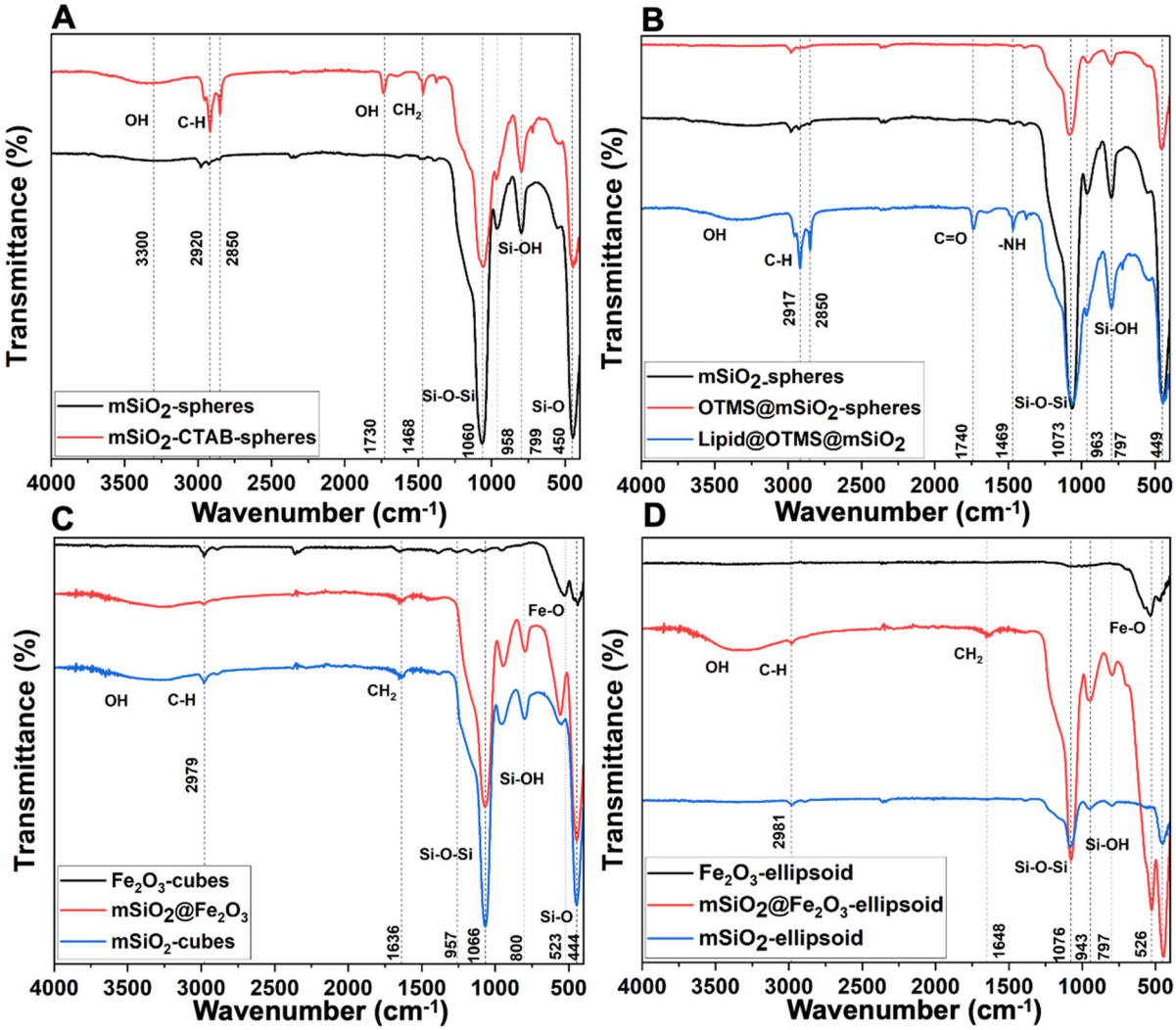

Fig. 4 Surface groups analysis by FTIR: (A) spectra of $mSiO_2$ indicate the removal of surfactant (CTAB) after HCl treatment. (B) Spectra after conjugation of OTMS highlights the disappearance of hydroxyl groups. While lipid-coated mesoporous silica nanocarriers show additional bands for –NH and C=O present in the lipid molecule. (C) α-Fe_2O_3 nanocubes (black), SiO_2@Fe_2O_3 core–shell cubes (red), and mesoporous silica cubes after α-Fe_2O_3 removal (blue). (D) α-Fe_2O_3 ellipsoid template (black), SiO_2@Fe_2O_3 core–shell ellipsoid (red) indicates the incorporation of silica shell, and mesoporous ellipsoid (blue) showcases a decrease in Fe–O characteristic peak at 526 cm^{-1} indicating the removal of the iron core.

drugs (tamoxifen) and kinase inhibitors (everolimus, bosutinib, and dasatinib) for the treatment of breast cancer, polycystic kidney disease (PKD), and Philadelphia chromosome-positive chronic myeloid leukemia (Ph + CML).[43,44]

The experimental data of drug entrapment showed that with the increase in molecular weight, a decrease in encapsulation efficacy was observed (Fig. 11A). This indicates that drug size impacts the loading capacity since molecules with larger molecular weight have reduced diffusion rates or encounter higher steric hindrance (van der Waals), resulting in different loading capacities with the change of molecular weight.

In addition to molecular weight, increased hydrophobicity of drug molecules also results in increased loading efficiencies, which is consistent with the observation that hydrophobic coating on $mSiO_2$ can promote drug uptake due to favorable hydrophobic–hydrophobic interactions (Fig. 11B).

Nanocarriers and cell interactions

The cell uptake study conducted with immune cells revealed that nanospheres exhibited the highest rate of cellular uptake compared to ellipsoids and cubes (Fig. 12). Furthermore, viability assays conducted with Peripheral Blood Mononuclear Cells (PBMCs) demonstrated that nanospheres and ellipsoids maintained similar cell viability, with both demonstrating 85% cell viability after 24 h incubation. In contrast, nanocubes showed the highest rate of cell death and apoptosis, with a reduced cell viability of 79% after the same duration (Fig. 13).

Nanocarrier uptake by cells predominantly occurs through endocytosis, including phagocytosis, pinocytosis, and notably, clathrin-mediated endocytosis. Clathrin-mediated endocytosis is a specific form of receptor-mediated uptake, where nanoparticles first bind to cell surface receptors and are then

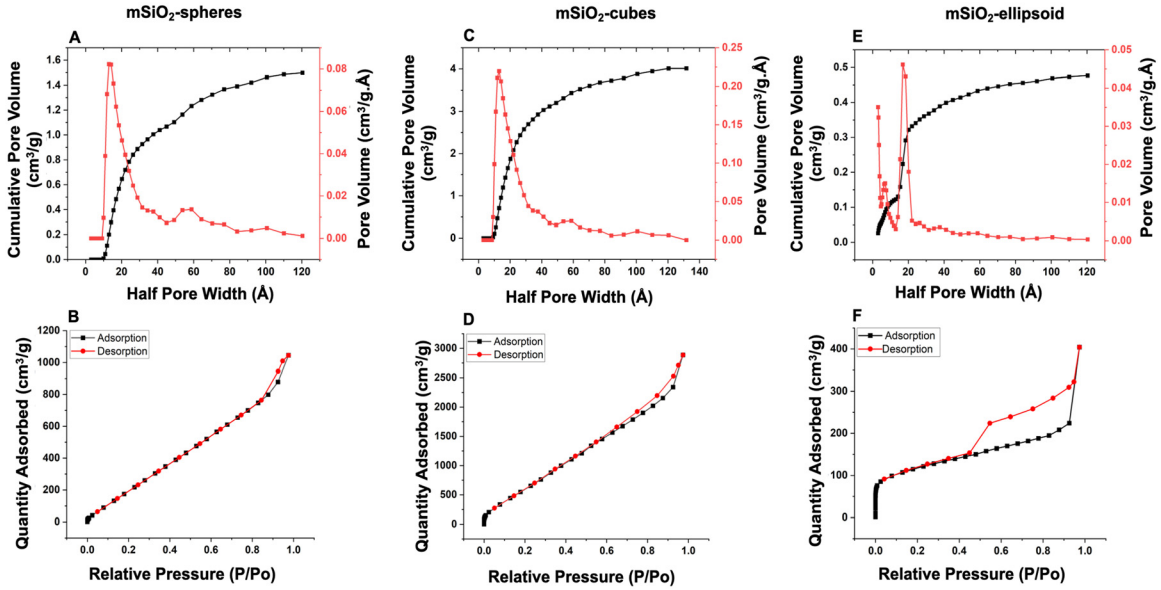

Fig. 5 Pore size distribution and surface area analysis by BET. (A, C and E) Pore size distribution and cumulative pore volume for mesoporous silica nanocarriers show a high concentration of half-width pores at around 18–20 Å (1.8–2 nm) suggesting uniformity in pore size across the samples. (B, D and F) Adsorption–desorption isotherms, follow a similar pattern for all nanocarriers where materials show a characteristic type IV isotherm with hysteresis, indicative of well-defined mesoporous structures.

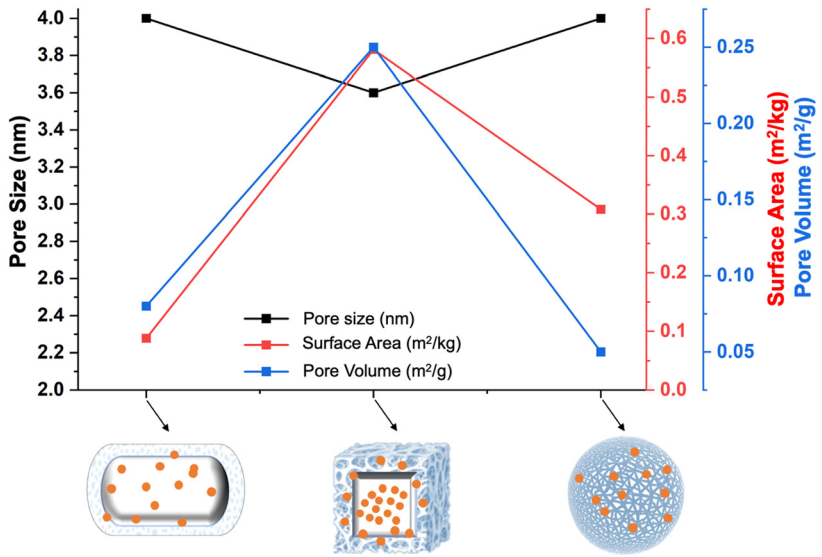

Fig. 6 Comparative analysis of pore size, surface area, and pore volume between nanospheres, nanocubes, and nanoellipsoids: nanospheres show a higher pore size (4 nm) while nanocubes on the other hand exhibited the highest surface area and slightly less pore size than nanospheres. The nanoellipsoids possess less surface area than cubes, however, they are larger than nanospheres. The pore volume for nanocubes (0.25 $cm^3\ g^{-1}$) is highest while nanoellipsoids exhibit the smallest pore volume (0.05 $cm^3\ g^{-1}$).

internalized within clathrin-coated vesicles. This pathway is especially significant for its selectivity and efficiency, facilitating the intracellular delivery of nanoparticle-bound therapeutics. The shape of the nanoparticles significantly influences this process. Small and spherical, nanoparticles are generally internalized more efficiently.[45,46] Zhang *et al.* elucidate the differential impact of nanocarrier morphology on cell uptake and cytotoxicity through a computational study focusing on how shapes affect endocytosis. Their findings revealed that spherical carriers were more efficiently internalized by immune cells compared to non-spherical counterparts. This enhanced efficiency is attributed to the compatibility of spherical shape with natural cellular intake processes, particularly, clathrin-mediated endocytosis, which is significantly influenced by the shape of particles.[47] Spherical nanocarriers, due to their shape, facilitate a more straightforward wrapping by

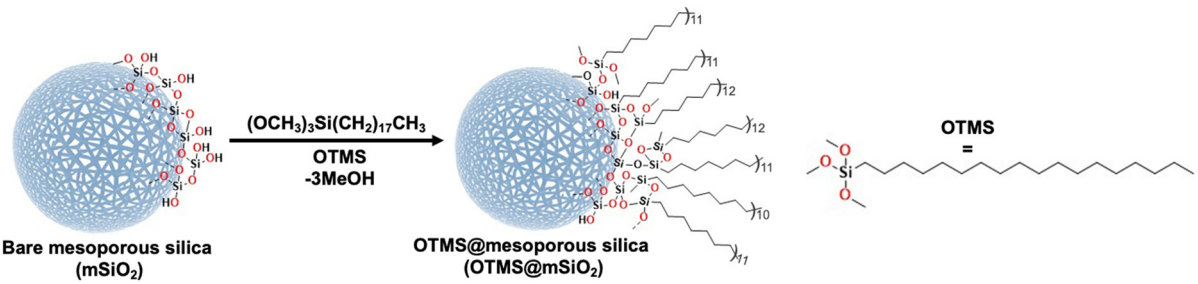

Scheme 1 Covalent conjugation of octadecyltrimethoxysilane (OTMS) on the surface of $mSiO_2$ nanocarriers.

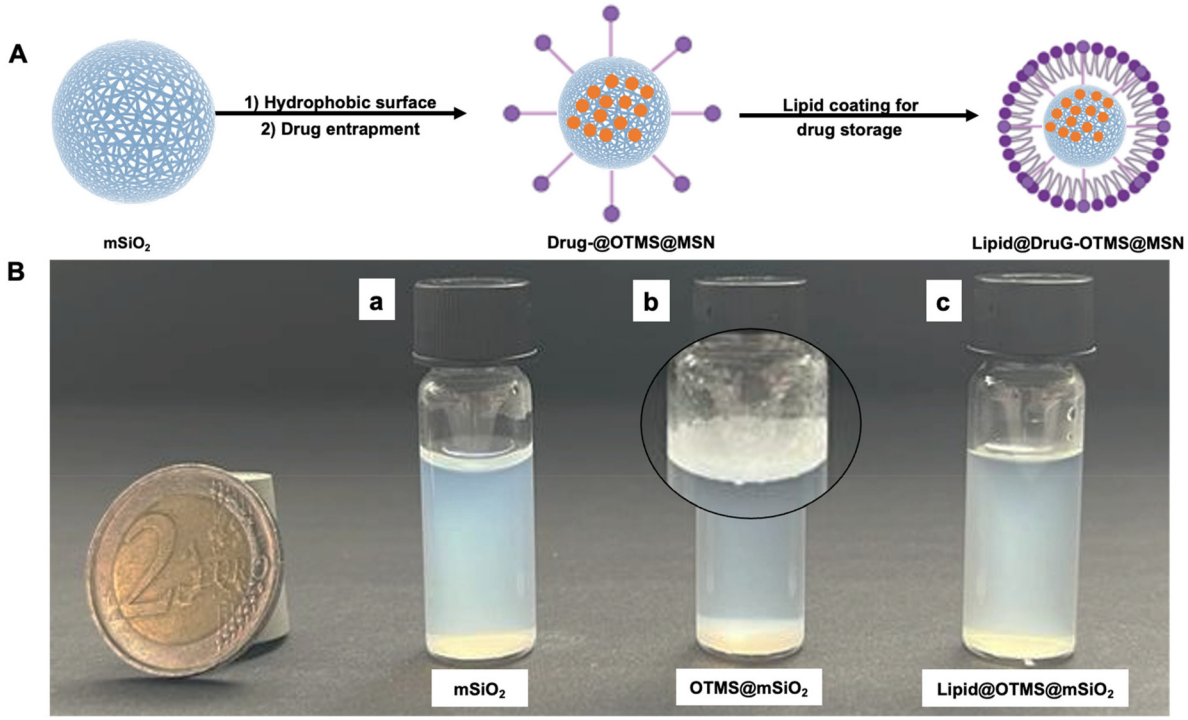

Fig. 7 (A) Schematic pathways for the synthesis of lipid-coated $mSiO_2$. Nanocarriers were modified with octadecyltrimethoxysilane. Further coating these nanocarriers with a lipid layer offered protection from uncontrolled drug release and stable nanodispersion. (B) Dispersion of nanocarriers in PBS (a) $mSiO_2$ were well dispersed in PBS (b) after surface conjugation linker molecule, the majority of the nanocarriers remained undispersed on the surface of PBS, indicating their hydrophobic nature. (c) After lipid coating nanocarriers were effectively dispersed in PBS.

the cell membrane, aided by the self-assembly of clathrins, as opposed to the more complex surfaces and angles of ellipsoids and cubes.

The process of clathrin-mediated endocytosis is highly sensitive to the shape of nanocarriers, and the efficiency of clathrin-mediated endocytosis as the shape anisotropy of the nanocarriers increases. Ellipsoids and cubes do not align well with the topology of clathrin structures, rendering them less efficient for internalization.[48,49] It is well documented that the rotation of nanocarriers during the endocytosis process influences their uptake affected by their orientation. Spherical nanocarriers exhibit reduced susceptibility to orientation issues due to their inherent isotropic symmetry. However, ellipsoids and nanocubes require a specific orientation for efficient membrane wrapping, with rotations potentially hindering the process. Additionally, encapsulating ellipsoids and cubic nanocarriers within cell membranes and clathrin structures necessitates significant deformation, requiring more energy, thus making the process less favorable for these shapes compared to spherical nanocarriers.[47–49]

This study provides a comprehensive overview of the properties of mesoporous silica nanocarriers and the effect of their distinct morphologies on potential biomedical applications, as outlined in Table 1. Consequently, it concludes that the careful selection and design of mesoporous silica nanocarriers, tailored to their specific morphological features, are imperative for enhancing therapeutic efficacy and achieving superior clinical outcomes for various medicinal applications.

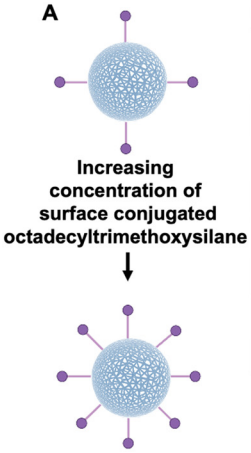

B

$mSiO_2$ [mg]	OTMS [mmolar]	OTMS (µl)	Tamoxifen concentration [mmolar]	Encapsulation efficiency [%]
20.0	1.40	5	0.151	44.7
20.0	6	25	0.151	45.3
20.0	12	50	0.151	56.6
20.0	23.57	100	0.151	32.3
20.0	47	200	0.151	36.8
20.0	94	400	0.151	38.6
20.0	118	500	0.151	25.1

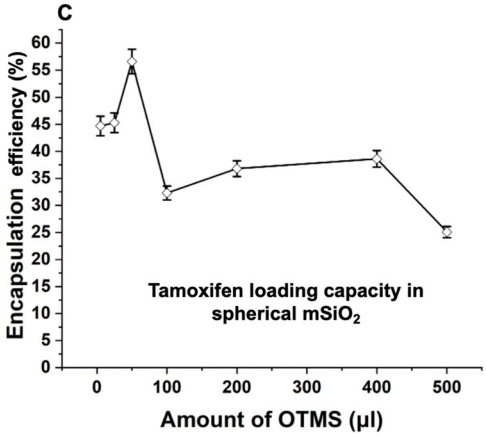

Fig. 8 Determination of drug loading capacity with an increasing concentration of surface-conjugated OTMS. (A) Hydrophobic silica carriers were synthesized by conjugating different concentrations of OTMS onto the surface of silica carriers. (B) A variable amount of OTMS was tested to determine the optimal conc. of linker. (C) With an increase in conjugated linker conc. loading capacity of $mSiO_2$ increased up to 50 µl and a further increase in conjugation of the linker decreased the entrapment efficacy. At higher linker concentrations the surface became saturated with functional groups, consequently providing reduced space for drug incorporation.

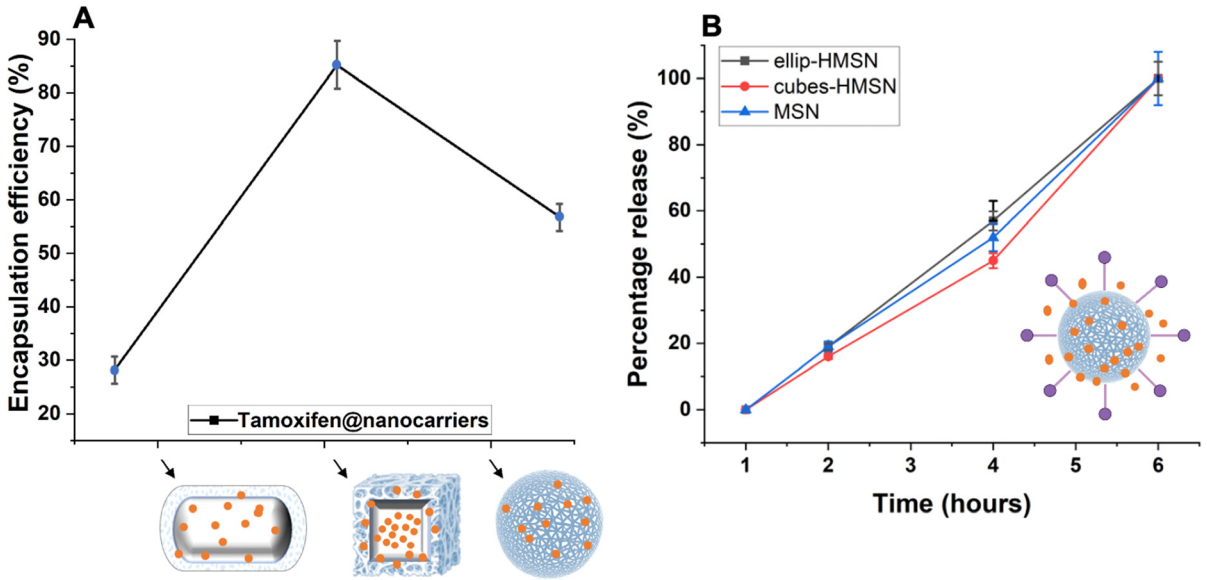

Fig. 9 Encapsulation efficiency of Tamoxifen in different HMSN: (influence of nanocarrier morphology). (A) Mesoporous cubes exhibited the highest drug loading capacity as compared to spherical, and ellipsoids due to a higher surface volume for the drug molecules. The lower loading capacity of spheres compared to the cubic shape can be due to their lower surface area as compared to cubes. The spherical nanoparticles have a more compact structure with limited surface area available for drug entrapment. (B) The release percentage of Tamoxifen: indicating the release of most of the drug within first six hours from all nanocarriers.

Materials and methods

Chemicals

All chemicals used in this study were of analytical grade and used without further purification. Iron(III) chloride hexahydrate ($FeCl_3{\cdot}6H_2O$, 97%), iron(III)nitrate nonahydrate ($Fe(NO_3)_3{\cdot}9H_2O$), ammonium hydroxide 30% solution (NH_4OH), cetyltrimethylammonium bromide (CTAB), tetraethyl orthosilicate (TEOS), triethanolamine (TEA) and tamoxifen were purchased from Sigma-Aldrich, di-ammonium hydrogen phosphate ($(NH_4)_2HPO_4$, 99+%) was procured from Merck. Dimethylformamide (DMF) was obtained from Fischer Scientific and poly(*N*-vinyl-2-pyrrolidone) MW = 55.000 (PVP) from Acros Organics. Octadecyl-trimethoxysilane obtained from TCI (Tokyo Chemical Industry). Everolimus, DPPC, and DSPE-PEG-NH_2 were purchased from BLDpharm. Bosutinib and dasatinib were purchased from Selleckchem. Phosphate-buffered saline (PBS) was obtained from Gibco. RPMI1640 medium, FBS, Penicillin/Streptomycin (Gibco); Annexin V binding buffer, Annexin V-APC (Biolegend), DAPI.

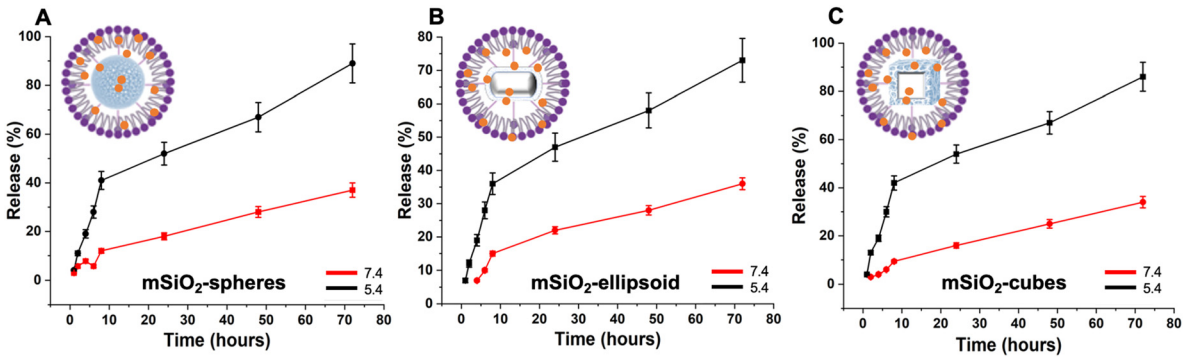

Fig. 10 Stimuli-responsive drug release study at different pH (7.4 and 5.4) (section Influence of nanocarrier morphology): (A–C) Tamoxifen release study from lipid-coated silica nanocarriers. The drug release was continuous and gradual over the entire 72-hour release period, indicating that the lipid coating effectively controlled the release of the loaded drugs.

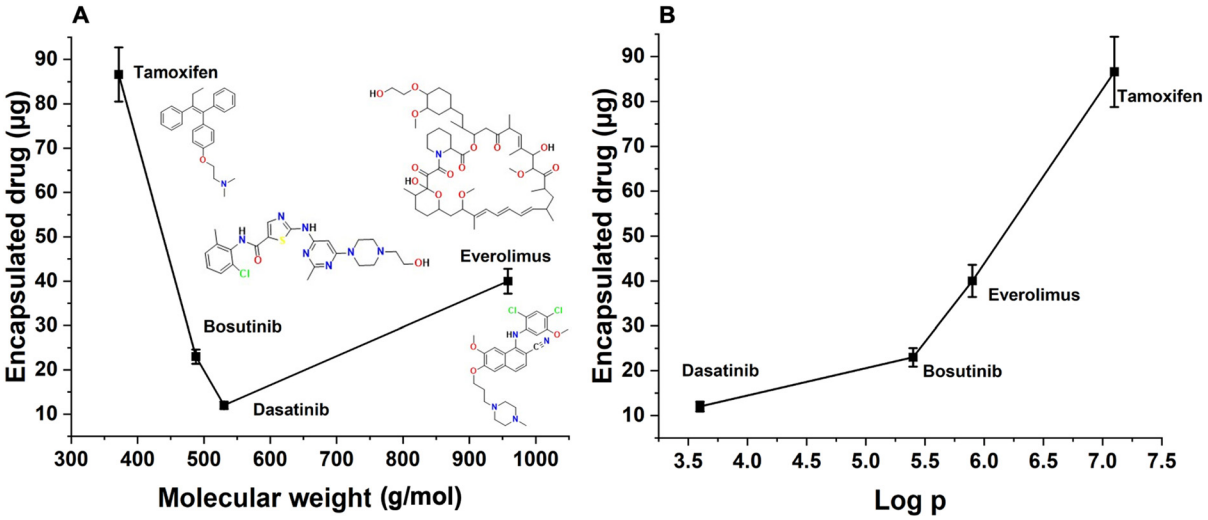

Fig. 11 Influence of drug characteristics on encapsulation efficiency. (A) Drug entrapment decreases with the increase in molecular weight as larger molecules have reduced diffusion rates or steric hindrance when attempting to penetrate the nanocarriers. (B) Increase in encapsulation efficiency of drug molecules with the increase in hydrophobicity due to interactions between the drugs and the hydrophobic regions of nanocarriers.

Antibodies (Biolegend): Anti Human CD3-APC/Cy7, Anti Human CD14-PE/Cy7, Anti Human CD20-PE. PBMCs from three healthy donors. Flow cytometer MACSQuant X (Mitenyi Biotec), analysis software Kaluza (Beckman Coulter).

Synthesis of mesoporous silica nanospheres

Mesoporous silica nanospheres ($mSiO_2$-nanospheres) were synthesized using a modified Stöber method.[50–52] Typically, a mixture of cetyltrimethylammonium bromide (CTAB) (1.852 g) and triethanolamine (TEA) (0.24 g) was added to 80 mL of water and heated to 80 °C in a flask fitted with a reflux condenser for 30 minutes. Subsequently, tetraethyl orthosilicate TEOS (1 mL) was added dropwise to the solution, resulting in a noticeable bluish-white color change. The reaction was allowed to proceed at 80 °C for 2 h and then cooled down to room temperature. The resulting white precipitate was separated by centrifugation at 11 000 rpm for 20 minutes, followed by washing with water and ethanol (3x) to obtain the mesoporous silica nanospheres.

Synthesis of iron oxide cubes

Iron oxide nanocubes were synthesized following a solvothermal reduction pathway published elsewhere.[53,54] Briefly, 0.8 g polyvinylpyrrolidone (PVP) was dissolved completely in 10 mL of *N*,*N*-dimethylformamide (DMF). PVP act as a stabilizer to regulate nucleation and growth uniformly across all axes preventing particle aggregation and kinetically controlling the growth of specific facets by binding onto others.[55,56] To the solution of PVP, iron nitrate nonahydrate dissolved in 14 mL of DMF was added and stirred until a homogeneous mixture resulted. The resulting mixture was then transferred to Teflon tubes and subjected to solvothermal treatment at a temperature of 180 °C for 30 h. After the solvothermal reaction, reddish precipitate was collected by centrifugation at

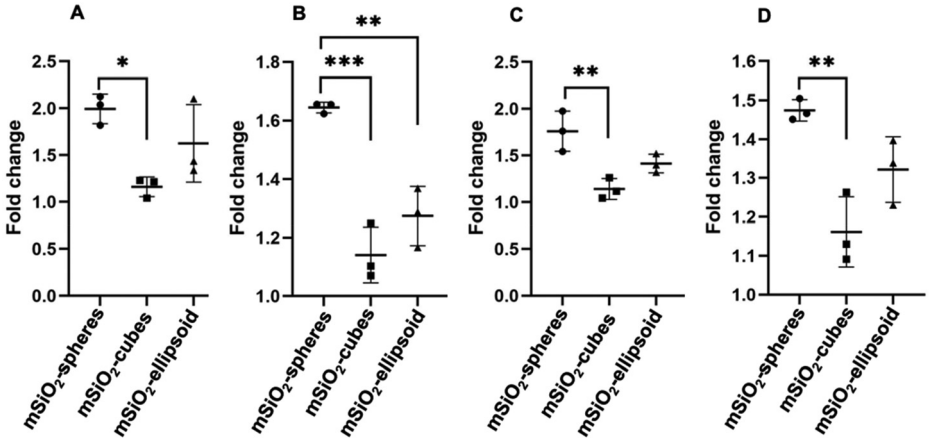

Fig. 12 Cell uptake analysis of different $mSiO_2$ shapes: the bar graphs depict the fold increase in cell uptake for $mSiO_2$ of different shapes (spheres, cubes, and ellipsoids) under two experimental conditions: (A and B) with consistent FITC concentration (0.1 μg mL^{-1}) for all three nanocarriers after 2 h and 4 h respectively. (C and D) and by standardizing the concentration of nanocarriers (20 μg mL^{-1}) for 2 h and 4 h respectively. All results showed a statistically significant higher fold increase in cell uptake for spheres compared to cubes and ellipsoids highlighting the influence of nanocarrier shape on cellular internalization efficiency.

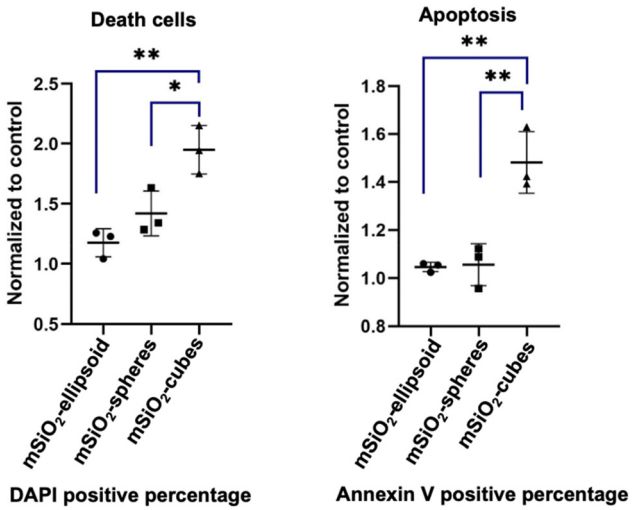

Fig. 13 Comparative analysis of cell death and apoptosis induced by different morphologies of $mSiO_2$ quantified through DAPI and Annexin V staining, respectively. Among the different shapes (ellipsoid, spheres, and cubes), $mSiO_2$-cubes have a notably higher capacity to induce cell death and apoptosis, as evidenced by increased levels of both DAPI-positive and Annexin V-positive cells. Following the cubes, mesoporous spheres exhibit intermediate effects, while ellipsoids are associated with the lowest level of toxicity. These results underscore the significant role that nanocarrier shape plays in biological interactions.

11 000 rpm for 30 minutes and washed with ethanol and acetone (5×) to remove any residual impurities. The obtained reddish nanoparticles were dried at 60 °C in a vacuum oven for further analysis.

Synthesis of iron oxide nanoellipsoids

Iron oxide nanoellipsoids were synthesized using a literature-reported method.[54] In brief, 1.3 g of iron chloride hexahydrate was dissolved in 204 mL of water with stirring until complete dissolution. To this iron chloride solution, ammonium hydrogen phosphate (13.2 mg) was added and stirred for 30 minutes to ensure complete mixing. The addition of ammonium hydrogen phosphate imparts directional growth, favoring elongation primarily along one axis, and adjusts the pH, influencing the condensation reactions of iron nitrate, and determining the final morphology and aspect ratio of the particles.[57–61]

The resulting mixture was then transferred to Teflon tubes and heated at 220 °C for 6 h. Following the reaction, reddish precipitates were obtained by centrifugation at 11 000 rpm for 20 minutes. The collected precipitates were then washed with water and ethanol (4 x) to remove any impurities and dried in an oven kept at 60 °C for further analysis and characterization.

Synthesis of mesoporous silica ellipsoids

For the synthesis of mesoporous silica particles, ellipsoidal iron oxide nanoparticles (72 mg) were used as hard templates. To a dispersion of iron oxide nanoellipsoids in 104 mL of water, freshly prepared silicic acid (720 μL), obtained by mixing 650 μL of TEOS with 5 mL of acidic water, was added and stirred for 10 minutes. Subsequently, 720 μL of ammonium hydroxide solution was added, and the mixture was stirred for an additional 10 minutes. This coating process was repeated once more and stirred at room temperature for 3 h. The coated nanoellipsoids obtained were separated by centrifugation at 9000 rpm for 15 minutes and washed with ethanol (3×) to obtain coated capsules dispersed in 72 mL of ethanol. TEOS (144 μL) was added dropwise to the dispersed nanocapsules under continuous stirring followed by the addition of 1.440 mL of ammonium hydroxide and stirring of the reaction mixture for 10 minutes. This coating process was repeated twice, and the resulting coated capsules were separated by centrifugation (11 000 rpm for 20 minutes) and washed with ethanol and water (3×). To remove the iron oxide template and obtain mesoporous silica capsules, the coated

Table 1 Characteristics and application of different silica-based nanocarriers

Nanocarriers	Pore size, nm	Size nm	Surface area, $m^2\ g^{-1}$	Concentration for cellular assays per mL	Cell viability % (24 h)	Out come
Spheres	4	60	88	≤50 μg	88.5	High drug encapsulation efficacy, low toxicity, high cellular uptake Suitable for drug delivery, as a diagnostic tool, theranostic application
Cubes	3.6	60	581.477	<50 μg	79.58	High loading efficacy but higher toxicity and lower uptake compared to ellipsoids and spheres Can be advantageous in the development of sensing devices, *in vitro* diagnostics, biosensors for pathogen detection, drug discovery, and development
Ellipsoid	4	200 × 100	323.8	≤300 μg	84.525	Low toxicity, efficient cell uptake and hight surface area. Targeted drug delivery Biosensors

capsules were treated with 12 molar hydrochloric acid (HCl) until the red color of the iron oxide completely disappeared. The obtained nanoparticles were washed with water and ethanol (3×) to remove HCl.

Synthesis of mesoporous silica cubes

A solution of CTAB (2 g) and triethylamine (20 mg) in water (20 mL), stirred for 1 hour, was added to a dispersion of iron oxide cubes (40 mg) in 10 mL of water. For the formation of silica shells, TEOS was added dropwise, and the resulting mixture was stirred at 80 °C for 1 hour. To obtain mesoporous silica cubes, the iron oxide cores, and CTAB templates were selectively removed by 12 molar HCl treatment until the disappearance of the red color. The resulting nanocubes were then collected *via* centrifugation (11 000 rpm for 20 minutes) and washed with ethanol and water (3×).

Characterization

The characterization of the synthesized products involved a comprehensive analysis utilizing multiple analytical techniques. Transmission Electron Microscopy (TEM) was conducted using a JEOL 2100 HR-(S) TEM instrument with a LaB_6 electron source operating at 200 kV, enabling nanoscale observation of the samples to determine their morphology and size. Scanning Electron Microscopy (SEM) measurements were performed using a Zeiss Sigma 300 VP microscope to obtain surface imaging and gather information regarding the surface morphology

The optical properties of the samples in the UV and visible regions were examined using Ultraviolet–Visible Spectroscopy (UV-Vis). UV-Vis spectra were acquired employing a CARY 50 Scan UV-Visible spectrometer to analyze the samples' absorbance properties. To investigate the functional groups, Fourier-Transform Infrared Spectroscopy (FTIR) measurements were recorded on a PerkinElmer FTIR spectrophotometer. X-ray Diffraction (XRD) analysis was performed on a Philips X'Pert diffractometer using Cu Kα radiation (λ = 1.504 nm) with a scan rate of $0.05°\ s^{-1}$ in the 2θ range of 10°–80°. This analysis enabled the determination of the crystalline structure of the samples, providing information about their crystallographic phases. Adsorption–desorption measurements (N_2 at 77 K) were performed to determine the porosity of all types of nanocarriers using an AUTOSORB-1-MP (Quantachrome). Before the adsorption–desorption measurements, all samples were heated to 100 °C under vacuum (1×10^{-7} mbar) for 20 hours to remove any adsorbed solvent. The Brunauer–Emmett–Teller (BET) surface area was calculated based on the pressure region P/P_0 = 0.05–0.25. To define the pore size distribution and volume, DFT calculations were performed using the cylindrical/sphere pore, NLDFT ads. model with a fitting error of 0.7%.

Surface functionalization of $mSiO_2$

The surface conjugation of all nanocarriers with a silane linker was performed by dispersing 100 mg of nanocarriers in 50 mL of ethanol under a nitrogen atmosphere at 60 °C. Subsequently, the hydrophobic linker (1.40, 6.0, 12.01, 23.57, 47.13, 94.27, 118 mmol) was added to the nanocarrier dispersion, and the mixture was stirred at 60 °C for 48 hours. Following this, the nanocarriers were collected by centrifugation at 11 000 rpm for 15 minutes and washed with ethanol to remove any unreacted linker and impurities.

Drug loading and release of silica nanocarriers

The drug-loading process for the nanocarriers involved a diffusion-based approach.[38] Specifically, tamoxifen-loaded silica nanocarriers were prepared by creating a 6 mL stock solution with a concentration of 0.151 mmol in ethanol. For bosutinib, dasatinib, and everolimus-loaded nanocarriers, stock solutions with the same concentration were prepared. After this step, the supernatant was then carefully and the concentration of the free drug in the supernatant was quantified using UV-Vis spectroscopy by utilizing a pre-established calibration curve of the drug (Fig. S5†). The drug-loaded nanocarriers were washed with ethanol using centrifugation (11 000 rpm, 10 minutes) to remove any drug molecules adsorbed on the surface. The encapsulation efficiency (EE) was calculated using the formula:

$$EE(\%) = ((\text{total drug} - \text{free drug})/\text{total drug}) \times 100,$$

where 'Total drug' is the initial amount of drug used in the synthesis, and 'Free drug' is the amount found in the supernatant.

Additionally, a drug release study was conducted under physiological conditions to verify the encapsulation, comparing the amount of drug released over time with the total encapsulated drug. To initiate drug release, 6 ml of release medium (ethanol : water (30 : 70)) was added to the drug-loaded nanocarriers. The system was then stirred in a water bath at a constant temperature of 37 °C for the desired duration of drug release. At various time intervals, the amount of released drug was determined by separating the supernatant (3 mL) through centrifugation (11 000 rpm, 10 minutes) and measuring the absorption data using UV-vis spectroscopy. To maintain a constant volume and obtain cumulative drug release profiles, an equal volume of fresh-release medium was added to the system.

Lipid coating on drug-loaded nanocarriers

An uncontrolled and abrupt release of drugs can be circumvented by coating the nanocarriers with a lipid layer. For lipid coating, a mixture of dipalmitoyl phosphatidylcholine (DPPC), cholesterol, and DSPE-PEG (2000)-NH_2 was prepared in a ratio of 13 : 6 : 1. The lipid mixture was then added to a suspension of drug-loaded nanocarriers in chloroform (1 mL). Subsequently, the chloroform was evaporated, and the lipid-nanocarriers mixture was dispersed in water (3 mL) and stirred at 40 °C for 4 hours to facilitate lipid coating. The lipid-coated nanocarriers were then purified by washing with water and subjected to centrifugation (11 000 rpm for 20 minutes). This washing process was repeated (3×) to ensure the removal of any excess lipids and impurities.

For the drug release study, the lipid-coated nanocarriers were dispersed in 6 mL of phosphate-buffered saline (PBS) and stirred in a water bath at a constant temperature of 37 °C. To investigate the drug release profile, the amount of released drug was periodically determined by separating the supernatant through centrifugation (11 000 rpm, 10 minutes) and measuring the absorption spectra using UV-Vis spectroscopy. To maintain a constant volume and obtain cumulative drug release profiles, an equal volume of fresh medium was added to the system after each measurement.

Cell uptake assay

Fluorescein (FITC) was encapsulated in all nanocarriers as a fluorescent dye to visualize the cells (Fig. S6†). Given the varying concentrations of FITC in different nanocarriers, cell uptake analysis was conducted both by keeping the concentration of nanocarrier consistent and as well by standardizing the concentration of FITC. Peripheral Blood Mononuclear Cells (PBMCs) were isolated from three healthy donors with the Institutional Review Board approvals at the University Hospital of Cologne no. 19-1559 (Buffy Coats) and no. 19–1438_1 and allowed to thaw for two hours before the treatment. Cell counts were performed using a MACSQuant X flow cytometer, followed by the dilution of cells to a concentration of 2 million cells per mL in complete RPMI medium (RPMI1640 + 10%FBS + 1% Penicillin/Streptomycin). For each assay, 50 μL of the PBMC solution was added to individual wells in a 96-well plate (10^5 cells per well). Dispersion of silica nanocarriers with different shapes was prepared in complete RPMI medium. These particles were then further diluted to final concentrations of 40 μg mL^{-1} for particles-based concentration and 0.2 μg mL^{-1} for FITC-based concentration. Subsequently, 50 μL of the nanocarrier solution was incubated with PBMCs, creating a good mixture with final concentrations of 20 μg mL^{-1} for particles-based concentration and 0.1 μg mL^{-1} for FITC-based concentration. All the tests were performed in duplicate for each nanocarrier shape. Plates were incubated to allow cellular uptake of nanocarriers, and after 2 hours and 4 hours, the cells were subjected to flow cytometry, utilizing strong vibration and a high-speed setting, with a uptake of 80 μL. Data analysis was performed using Kaluza Analysis software, targeting the identification of FITC-positive cells, and results were graphed and statistically analyzed using GraphPad Prism version 8, depicting the fold change in the uptake of the different morphologies of nanocarriers by the PBMCs.

Cytotoxicity of nanoparticles

Immune cell-type PBMCs were isolated from three healthy donors and seeded in 96 well plates (10^5 cells per well) and co-incubated with nanocarrier suspension (50 μL, 1 mg per 1 mL) of mesoporous spheres, cubes, and ellipsoid for 24 hours. After 24 hours antibody solution containing Annexin V binding buffer (10 μL per well), Annexin V APC (0.2 μL per well), DAPI (0.002 μL per well) (1 : 50.000 dilution ratio), Anti-human CD3-APC Cy7 (0.2 μL per well), Anti-human CD14- PE/Cy7 (0.2 μL per well), Anti-human CD20-PE (0.2 μL per well) was added to each well and incubate for 20 minutes. After incubation time, flow cytometry was performed to identify apoptotic and dead cells by using strong vibration, high speed, with a volume of 80 μL. The data was then analyzed with Kaluza Analysis software to detect Annexin V-positive and DAPI-positive cells. This analysis was applied to the cells in total and specific cell populations including $CD3^+$(T cells), $CD20^+$(B cells), and $CD14^+$ myeloid cells.

Conclusions

This study demonstrates the potential of mesoporous silica nanocarriers modified with OTMS and sealed with a lipid layer as a promising approach for enhanced storage and sustained release of hydrophobic drugs over prolonged durations. The morphology of nanocarriers was found to notably impact the storage and entrapment of hydrophobic drugs, with mesoporous nanocubes exhibiting superior loading capacity due to their higher surface area and porosity compared to alternative nanocarriers such as mesoporous nanoellipsoids, and nanospheres. Furthermore, achieving optimal drug entrapment within the nanocarriers depends not solely on the nanocarrier shape but also on the molecular weight and hydrophobic nature of the drug. The high surface area and the optimal pore

size of the cubic particles contribute to their highest drug-loading capacity. While spherical nanocarriers showed the highest biocompatibility and minimal toxicity against immune cells, they also exhibited superior cellular uptake owing to their uniform shape. These findings offer critical insights into the design of nanocarrier-based drug delivery systems tailored for hydrophobic drugs. Our findings underscore the importance of considering both nanocarrier morphology and drug properties to achieve optimal drug loading capacities and precise controlled release into the surrounding medium.

Author contributions

Sumiya Iqbal conducted the experimental work, evaluated, and deduced the results, and wrote the complete manuscript. Tom-Jonas Klaus Schneider synthesized ellipsoid nanoparticles and assisted in their analysis. Thanh Tung Truong conducted the cell tests and analyzed and proofread the cell assays. Roman Ulrich-Müller, Phuong-Hien Nguyen are collaborating partners on the project and assisted bosutinib, dasatinib, and everolimus, and proofread the manuscript. Prof. Sanjay Mathur and Dr. Shaista Ilyas discussed the concept of the research work, supervised the experimental work, and contributed to the writing of the manuscript and discussions throughout the study.

Conflicts of interest

The authors declare no competing financial interest.

Acknowledgements

The authors thank the University of Cologne for infrastructural and financial support in the framework of the UoC Forum, iRNA-Carriers "Transformative Nanocarriers for RNA Transport and Tracking." We gratefully acknowledge Prof. Uwe Ruschewitz and Ronja Christoffels for their help in performing the BET analysis of nanocarriers. Ms Nurgül Tosun and is acknowledged for her support in performing the TEM analysis of our nanoparticle samples. A doctoral research fellowship by DAAD (Grant No. 57552340) to Ms Iqbal is thankfully acknowledged.

References

1 A. Ubeyitogullari and O. N. Ciftci, A Novel and Green Nanoparticle Formation Approach to Forming Low-Crystallinity Curcumin Nanoparticles to Improve Curcumin's Bioaccessibility, *Sci. Rep.*, 2019, **9**(1), 19112, DOI: **10.1038/s41598-019-55619-4**.

2 N. Shrivastava, A. Parikh, R. P. Dewangan, L. Biswas, A. K. Verma, S. Mittal, J. Ali, S. Garg and S. Baboota, Solid Self-Nano Emulsifying Nanoplatform Loaded with Tamoxifen and Resveratrol for Treatment of Breast Cancer, *Pharmaceutics*, 2022, **14**(7), 1486, DOI: **10.3390/pharmaceutics14071486**.

3 V. S. Ipar, A. Dsouza and P. V. Devarajan, Enhancing Curcumin Oral Bioavailability Through Nanoformulations, *Eur. J. Drug Metab. Pharmacokinet.*, 2019, 459–480, DOI: **10.1007/s13318-019-00545-z**.

4 P. Dehghankelishadi, P. Badiee, M. F. Maritz, N. Dmochowska and B. Thierry, Bosutinib High Density Lipoprotein Nanoformulation Has Potent Tumour Radiosensitisation Effects, *J. Nanobiotechnol.*, 2023, **21**(1), 102, DOI: **10.1186/s12951-023-01848-9**.

5 S. Satapathy and C. S. Patro, Solid Lipid Nanoparticles for Efficient Oral Delivery of Tyrosine Kinase Inhibitors: A Nano Targeted Cancer Drug Delivery, *Adv. Pharm. Bull.*, 2022, 298–308, DOI: **10.34172/apb.2022.041**.

6 A. Siew, H. Le, M. Thiovolet, P. Gellert, A. Schatzlein and I. Uchegbu, Enhanced Oral Absorption of Hydrophobic and Hydrophilic Drugs Using Quaternary Ammonium Palmitoyl Glycol Chitosan Nanoparticles, *Mol. Pharm.*, 2012, **9**(1), 14–28, DOI: **10.1021/mp200469a**.

7 A. K. Varma, R. Patil, S. Das, A. Stanley, L. Yadav and A. Sudhakar, Optimized Hydrophobic Interactions and Hydrogen Bonding at the Target-Ligand Interface Leads the Pathways of Drug-Designing, *PLoS One*, 2010, **5**(8), 12029, DOI: **10.1371/journal.pone.0012029**.

8 G. Yang, Y. Liu, H. Wang, R. Wilson, Y. Hui, L. Yu, D. Wibowo, C. Zhang, A. K. Whittaker, A. P. J. Middelberg and C. X. Zhao, Bioinspired Core–Shell Nanoparticles for Hydrophobic Drug Delivery, *Angew. Chem., Int. Ed.*, 2019, **58**(40), 14357–14364, DOI: **10.1002/anie.201908357**.

9 F. Ditzinger, D. J. Price, A. R. Ilie, N. J. Köhl, S. Jankovic, G. Tsakiridou, S. Aleandri, L. Kalantzi, R. Holm, A. Nair, C. Saal, B. Griffin and M. Kuentz, Lipophilicity and Hydrophobicity Considerations in Bio-Enabling Oral Formulations Approaches – a PEARRL Review, *J. Pharm. Pharmacol.*, 2019, 464–482, DOI: **10.1111/jphp.12984**.

10 L. L. Lou and J. C. Martin, Selected Thoughts on Hydrophobicity in Drug Design, *Molecules*, 2021, **26**(4), 875, DOI: **10.3390/molecules26040875**.

11 P. Liu, G. Chen and J. Zhang, A Review of Liposomes as a Drug Delivery System: Current Status of Approved Products, Regulatory Environments, and Future Perspectives, *Molecules*, 2022, 1372, DOI: **10.3390/molecules27041372**.

12 Y. Su, B. Zhang, R. Sun, W. Liu, Q. Zhu, X. Zhang, R. Wang and C. Chen, PLGA-Based Biodegradable Microspheres in Drug Delivery: Recent Advances in Research and Application, *Drug Delivery*, 2021, **28**(1), 1397–1418, DOI: **10.1080/10717544.2021.1938756**.

13 J. German-Cortés, M. Vilar-Hernández, D. Rafael, I. Abasolo and F. Andrade, Solid Lipid Nanoparticles: Multitasking Nano-Carriers for Cancer Treatment, *Pharmaceutics*, 2023, **15**(3), 831, DOI: **10.3390/pharmaceutics15030831**.

14 M. Zenze, A. Daniels and M. Singh, Dendrimers as Modifiers of Inorganic Nanoparticles for Therapeutic Delivery in Cancer, *Pharmaceutics*, 2023, **15**(2), 398, DOI: **10.3390/pharmaceutics15020398**.

15 R. Sakthi Devi, A. Girigoswami, M. Siddharth and K. Girigoswami, Applications of Gold and Silver Nanoparticles in Theranostics, *Appl. Biochem. Biotechnol.*, 2022, 4187–4219, DOI: 10.1007/s12010-022-03963-z.

16 E. B. Lim, T. A. Vy and S. W. Lee, Comparative Release Kinetics of Small Drugs (Ibuprofen and Acetaminophen) from Multifunctional Mesoporous Silica Nanoparticles, *J. Mater. Chem. B*, 2020, **8**(10), 2096–2106, DOI: 10.1039/c9tb02494h.

17 Z. Yi, L. F. Dumée, C. J. Garvey, C. Feng, F. She, J. E. Rookes, S. Mudie, D. M. Cahill and L. Kong, A New Insight into Growth Mechanism and Kinetics of Mesoporous Silica Nanoparticles by in Situ Small Angle X-Ray Scattering, *Langmuir*, 2015, **31**(30), 8478–8487, DOI: 10.1021/acs.langmuir.5b01637.

18 N. S. Zaharudin, E. D. Mohamed Isa, H. Ahmad, M. B. Abdul Rahman and K. Jumbri, Functionalized Mesoporous Silica Nanoparticles Templated by Pyridinium Ionic Liquid for Hydrophilic and Hydrophobic Drug Release Application, *J. Saudi Chem. Soc.*, 2020, **24**(3), 289–302, DOI: 10.1016/j.jscs.2020.01.003.

19 Y. Wang, S. Xiao, J. Xu and D. Lin, Mechanism of the Insecticidal Effect of Lambda-Cyhalothrin Loaded Mesoporous Silica Nanoparticles with Different Sizes and Surface Modifications on Ostrinia Furnacalis (Guenée) Larvae, *J. Zhejiang Univ., Sci., A*, 2023, 465–472, DOI: 10.1631/jzus.A2200334.

20 C. Deng, Y. Liu, F. Zhou, M. Wu, Q. Zhang, D. Yi, W. Yuan and Y. Wang, Engineering of Dendritic Mesoporous Silica Nanoparticles for Efficient Delivery of Water-Insoluble Paclitaxel in Cancer Therapy, *J. Colloid Interface Sci.*, 2021, **593**, 424–433, DOI: 10.1016/j.jcis.2021.02.098.

21 S. Ilyas, N. K. Ullah, M. Ilyas, K. Wennhold, M. Iqbal, H. A. Schlößer, M. S. Hussain and S. Mathur, Mediating the Fate of Cancer Cell Uptake: Dual-Targeted Magnetic Nanovectors with Biotin and Folate Surface Ligands, *ACS Biomater. Sci. Eng.*, 2020, **6**(11), 6138–6147, DOI: 10.1021/acsbiomaterials.0c00771.

22 A. M. Renner, S. Ilyas, H. A. Schlößer, A. Szymura, S. Roitsch, K. Wennhold and S. Mathur, Receptor-Mediated in Vivo Targeting of Breast Cancer Cells with 17α-Ethynylestradiol-Conjugated Silica-Coated Gold Nanoparticles, *Langmuir*, 2020, **36**(48), 14819–14828, DOI: 10.1021/acs.langmuir.0c02820.

23 M. Gisbert-Garzaran, D. Lozano, K. Matsumoto, A. Komatsu, M. Manzano, F. Tamanoi and M. Vallet-Regi, Designing Mesoporous Silica Nanoparticles to Overcome Biological Barriers by Incorporating Targeting and Endosomal Escape, *ACS Appl. Mater. Interfaces*, 2021, **13**(8), 9656–9666, DOI: 10.1021/acsami.0c21507.

24 A. E. LaBauve, T. E. Rinker, A. Noureddine, R. E. Serda, J. Y. Howe, M. B. Sherman, A. Rasley, C. J. Brinker, D. Y. Sasaki and O. A. Negrete, Lipid-Coated Mesoporous Silica Nanoparticles for the Delivery of the ML336 Antiviral to Inhibit Encephalitic Alphavirus Infection, *Sci. Rep.*, 2018, **8**(1), 13990, DOI: 10.1038/s41598-018-32033-w.

25 A. K. Singh, S. S. Singh, A. S. Rathore, S. P. Singh, G. Mishra, R. Awasthi, S. K. Mishra, V. Gautam and S. K. Singh, Lipid-Coated MCM-41 Mesoporous Silica Nanoparticles Loaded with Berberine Improved Inhibition of Acetylcholine Esterase and Amyloid Formation, *ACS Biomater. Sci. Eng.*, 2021, **7**(8), 3737–3753, DOI: 10.1021/acsbiomaterials.1c00514.

26 A. K. Pada, D. Desai, K. Sun, N. P. Govardhanam, K. Törnquist, J. Zhang and J. M. Rosenholm, Comparison of Polydopamine-Coated Mesoporous Silica Nanorods and Spheres for the Delivery of Hydrophilic and Hydrophobic Anticancer Drugs, *Int. J. Mol. Sci.*, 2019, **20**(14), 3408, DOI: 10.3390/ijms20143408.

27 A. M. Renner, M. B. Schütz, D. Moog, T. Fischer and S. Mathur, Electroacoustic Quantification of Surface Bound Ligands in Functionalized Silica and Iron Oxide Nanoparticles, *ChemistrySelect*, 2019, **4**(40), 11959–11964, DOI: 10.1002/slct.201902710.

28 S. Iranpour, A. R. Bahrami, S. Nekooei, A. Sh. Saljooghi and M. M. Matin, Improving Anti-Cancer Drug Delivery Performance of Magnetic Mesoporous Silica Nanocarriers for More Efficient Colorectal Cancer Therapy, *J. Nanobiotechnol.*, 2021, **19**(1), 1–22, DOI: 10.1186/s12951-021-01056-3.

29 F. Chen, H. Hong, S. Shi, S. Goel, H. F. Valdovinos, R. Hernandez, C. P. Theuer, T. E. Barnhart and W. Cai, Engineering of Hollow Mesoporous Silica Nanoparticles for Remarkably Enhanced Tumor Active Targeting Efficacy, *Sci. Rep.*, 2014, **4**, 1–10, DOI: 10.1038/srep05080.

30 X. Hong, X. Zhong, G. Du, Y. Hou, Y. Zhang, Z. Zhang, T. Gong, L. Zhang and X. Sun, *The Pore Size of Mesoporous Silica Nanoparticles Regulates Their Antigen Delivery Efficiency*, 2020, **6**(25), eaaz4462. https://www.science.org.

31 I. Gessner, E. Krakor, A. Jurewicz, V. Wulff, L. Kling, S. Christiansen, N. Brodusch, R. Gauvin, L. Wortmann, M. Wolke, G. Plum, A. Schauss, J. Krautwurst, U. Ruschewitz, S. Ilyas and S. Mathur, Hollow Silica Capsules for Amphiphilic Transport and Sustained Delivery of Antibiotic and Anticancer Drugs, *RSC Adv.*, 2018, **8**(44), 24883–24892, DOI: 10.1039/c8ra03716g.

32 E. Krakor, S. Saniternik, I. Gessner, R. Frohnhoven, M. Wilhelm, M. Drexelius, N. Tosun, I. Neundorf and S. Mathur, Hollow Mesoporous Silica Capsules Loaded with Copper, Silver, and Zinc Oxide Nanoclusters for Sustained Antibacterial Efficacy, *J. Am. Ceram. Soc.*, 2022, **105**(3), 1685–1696, DOI: 10.1111/jace.18002.

33 H. Kanniyappan, J. Jose, S. Chakraborty, M. Ramasamy and V. Muthuvijayan, PH-Responsive, Drug Release from Positively Charged Mesoporous Silica Nanoparticles and Their Potential for Anticancer Drug Delivery, *J. Aust. Ceram. Soc.*, 2023, **59**(1), 207–220, DOI: 10.1007/s41779-022-00827-x.

34 L. Xiao, M. Mertens, L. Wortmann, S. Kremer, M. Valldor, T. Lammers, F. Kiessling and S. Mathur, Enhanced in Vitro and in Vivo Cellular Imaging with Green Tea Coated Water-Soluble Iron Oxide Nanocrystals, *ACS Appl. Mater. Interfaces*, 2015, **7**(12), 6530–6540, DOI: 10.1021/am508404t.

35 A. A. Alotaibi, A. K. Shukla, M. H. Mrad, A. M. Alswieleh and K. M. Alotaibi, Fabrication of Polysulfone-Surface Functionalized Mesoporous Silica Nanocomposite Membranes for Removal of Heavy Metal Ions from Wastewater, *Membranes*, 2021, **11**(12), 935, DOI: **10.3390/membranes11120935**.

36 O. A. Saputra, W. A. Lestari, V. Kurniansyah, W. W. Lestari, T. Sugiura, R. R. Mukti, R. Martien and F. R. Wibowo, Organically Surface Engineered Mesoporous Silica Nanoparticles Control the Release of Quercetin by PH Stimuli, *Sci. Rep.*, 2022, **12**(1), 20661, DOI: **10.1038/s41598-022-25095-4**.

37 K. H. Kim, D. J. Lee, K. M. Cho, S. J. Kim, J. K. Park and H. T. Jung, Complete Magnesiothermic Reduction Reaction of Vertically Aligned Mesoporous Silica Channels to Form Pure Silicon Nanoparticles, *Sci. Rep.*, 2015, **5**, 9014, DOI: **10.1038/srep09014**.

38 C. G. Bavnhøj, M. M. Knopp, C. M. Madsen and K. Löbmann, The Role Interplay between Mesoporous Silica Pore Volume and Surface Area and Their Effect on Drug Loading Capacity, *Int. J. Pharm.: X*, 2019, **1**, 100008, DOI: **10.1016/j.ijpx.2019.100008**.

39 T. Yu, K. Greish, L. D. McGill, A. Ray and H. Ghandehari, Influence of Geometry, Porosity, and Surface Characteristics of Silica Nanoparticles on Acute Toxicity: Their Vasculature Effect and Tolerance Threshold, *ACS Nano*, 2012, **6**(3), 2289–2301, DOI: **10.1021/nn2043803**.

40 X. Cai, B. Fan, S. H. Thang, C. J. Drummond, N. Tran and J. Zhai, Paclitaxel-Loaded Cubosome Lipid Nanocarriers Stabilised with PH and Hydrogen Peroxide-Responsive Steric Stabilisers as Drug Delivery Vehicles, *J. Mater. Chem. B*, 2022, **11**(2), 403–414, DOI: **10.1039/d2tb01530g**.

41 Y. Cao, J. Zhu, J. Kou, D. P. Tieleman and Q. Liang, Unveiling Interactions of Tumor-Targeting Nanoparticles with Lipid Bilayers Using a Titratable Martini Model, *J. Chem. Theory Comput.*, 2024, DOI: **10.1021/acs.jctc.4c00231**.

42 E. Yuba, T. Osaki, M. Ono, S. Park, A. Harada, M. Yamashita, K. Azuma, T. Tsuka, N. Ito, T. Imagawa and Y. Okamoto, Bleomycin-Loaded PH-Sensitive Polymer-Lipid-Incorporated Liposomes for Cancer Chemotherapy, *Polymers*, 2018, **10**(1), 74, DOI: **10.3390/polym10010074**.

43 A. Cox, M. Tung, H. Li, K. R. Hallows and E. J. Chung, In Vitro Delivery of MTOR Inhibitors by Kidney-Targeted Micelles for Autosomal Dominant Polycystic Kidney Disease, *SLAS Technol.*, 2023, **28**(4), 223–229, DOI: **10.1016/j.slast.2023.02.001**.

44 B. Muresan, C. Mamolo, J. C. Cappelleri, E. Leip, A. Viqueira and B. Heeg, An Indirect Comparison between Bosutinib, Nilotinib and Dasatinib in First-Line Chronic Phase Chronic Myeloid Leukemia, *Curr. Med. Res. Opin.*, 2021, **37**(5), 801–809, DOI: **10.1080/03007995.2021.1896489**.

45 N. D. Donahue, H. Acar and S. Wilhelm, Concepts of Nanoparticle Cellular Uptake, Intracellular Trafficking, and Kinetics in Nanomedicine, *Adv. Drug Delivery Rev.*, 2019, 68–96, DOI: **10.1016/j.addr.2019.04.008**.

46 S. Behzadi, V. Serpooshan, W. Tao, M. A. Hamaly, M. Y. Alkawareek, E. C. Dreaden, D. Brown, A. M. Alkilany, O. C. Farokhzad and M. Mahmoudi, Cellular Uptake of Nanoparticles: Journey inside the Cell, *Chem. Soc. Rev.*, 2017, 4218–4244, DOI: **10.1039/c6cs00636a**.

47 Y. Li, M. Zhang, Y. Zhang, X. Niu, Z. Liu, T. Yue and W. Zhang, A Computational Study of the Influence of Nanoparticle Shape on Clathrin-Mediated Endocytosis, *J. Mater. Chem. B*, 2023, **11**(27), 6319–6334, DOI: **10.1039/d3tb00322a**.

48 M. Haripriyaa and K. Suthindhiran, Pharmacokinetics of Nanoparticles: Current Knowledge, Future Directions and Its Implications in Drug Delivery, *Future J. Pharm. Sci.*, 2023, **9**(1), 113, DOI: **10.1186/s43094-023-00569-y**.

49 S. Niaz, B. Forbes and B. T. Raimi-Abraham, Exploiting Endocytosis for Non-Spherical Nanoparticle Cellular Uptake, *Nanomanufacturing*, 2022, **2**(1), 1–16, DOI: **10.3390/nanomanufacturing2010001**.

50 M. Khoeini, A. Najafi, H. Rastegar and M. Amani, Improvement of Hollow Mesoporous Silica Nanoparticles Synthesis by Hard-Templating Method via CTAB Surfactant, *Ceram. Int.*, 2019, **45**(10), 12700–12707, DOI: **10.1016/j.ceramint.2019.03.125**.

51 S. Dong, Z. Feng, R. Ma, T. Zhang, J. Jiang, Y. Li, Y. Zhang, S. Li, X. Liu, X. Liu and H. Meng, Engineered Design of a Mesoporous Silica Nanoparticle-Based Nanocarrier for Efficient MRNA Delivery in Vivo, *Nano Lett.*, 2023, **23**(6), 2137–2147, DOI: **10.1021/acs.nanolett.2c04486**.

52 M. B. Schütz, S. Ilyas, K. Lê, M. Valldor and S. Mathur, Nanoparticle Arrays Having Directed Hybrid Topology via Covalent Self-Assembly of Iron Oxide and Silica Nanoparticles, *ACS Appl. Nano Mater.*, 2020, **3**(6), 5936–5943, DOI: **10.1021/acsanm.0c01097**.

53 H. Yin, Q. Yan, Y. Liu, L. Yang, Y. Liu, Y. Luo, T. Chen, N. Li and M. Wu, Co-Encapsulation of Paclitaxel and 5-Fluorouracil in Folic Acid-Modified, Lipid-Encapsulated Hollow Mesoporous Silica Nanoparticles for Synergistic Breast Cancer Treatment, *RSC Adv.*, 2022, **12**(50), 32534–32551, DOI: **10.1039/d2ra03718a**.

54 S. Ilyas, E. M. Sahnoun, S. A. Szymura, J. Pes, S. Habib, A. Florea, L. Schäfer, E. M. Buhl, A. Morgenroth, P. Habib, F. M. Mottaghy and S. Mathur, Validation of Dual-Action Chemo-Radio-Labeled Nanocarriers with High Efficacy against Triple-Negative Breast Cancer, *ACS Appl. Mater. Interfaces*, 2023, **15**(42), 48963–48977, DOI: **10.1021/acsami.3c10579**.

55 R. Ortega-Córdova, K. Sánchez-Carrillo, S. Carrasco-Saavedra, G. Ramírez-García, M. G. Pérez García, J. F. A. Soltero Martínez and J. D. Mota-Morales, Polyvinylpyrrolidone-Mediated Synthesis of Ultra-Stable Gold Nanoparticles in Nonaqueous Choline Chloride – Urea Deep Eutectic Solvent, *RSC Appl. Interfaces*, 2024, DOI: **10.1039/d3lf00261f**.

56 K. M. Koczkur, S. Mourdikoudis, L. Polavarapu and S. E. Skrabalak, Polyvinylpyrrolidone (PVP) in Nanoparticle Synthesis, *Dalton Trans.*, 2015, **44**(41), 17883–17905, DOI: **10.1039/c5dt02964c**.

57 C. Cheng, K. Tong, Y. Fang, J. Wang, Y. Liu and J. Tan, Ammonium-Induced Synthesis of Highly Fluorescent Hydroxyapatite Nanoparticles with Excellent Aqueous Colloidal Stability for Secure Information Storage, *Coatings*, 2019, **9**(5), 289, DOI: **10.3390/coatings9050289**.

58 S. Ebrahimi, C. S. S. Mohd Nasri and S. E. Bin Arshad, Hydrothermal Synthesis of Hydroxyapatite Powders Using Response Surface Methodology (RSM), *PLoS One*, 2021, **16**(5 May), e0251009, DOI: **10.1371/journal.pone.0251009**.

59 X. Zhang, Y. Niu, Y. Yang, Y. Li and J. Zhao, Preparation and Magnetic Properties of γ-Fe2O 3@SiO_2 Core Shell Ellipsoids with Different Aspect Ratios, *New J. Chem.*, 2014, **38**(9), 4351–4356, DOI: **10.1039/c4nj00389f**.

60 T. Ding, Z. Liu, K. Song and C. H. Tung, Synthesis of Monodisperse Ellipsoids with Tunable Aspect Ratios, *Colloids Surf., A*, 2009, **336**(1–3), 29–34, DOI: **10.1016/j.colsurfa.2008.11.007**.

61 A. Zeeshan, H. Hadji, H. Khelifa, M. Bourge and K. Bouchemal, Understanding the Interplay between Surface Properties and the Aspect Ratio of Ellipsoidal Nanomaterials, *Colloids Surf., A*, 2024, **680**, DOI: **10.1016/j.colsurfa.2023.132680**.